

# Design of mid-infrared amplifiers based on fiber taper coupling to erbium-doped microspherical resonator

Luciano Mescia,\* Pietro Bia, Marco De Sario, Annalisa Di Tommaso,  
and Francesco Prudeniano

DEE-Dipartimento di Elettrotecnica ed Elettronica, Politecnico di Bari,  
via E. Orabona 4, 70125 Bari - Italy

\*[mescia@deemail.poliba.it](mailto:mescia@deemail.poliba.it)

**Abstract:** A dedicated 3D numerical model based on coupled mode theory and solving the rate equations has been developed to analyse, design and optimize an optical amplifier obtained by using a tapered fiber and a  $\text{Er}^{3+}$ -doped chalcogenide microsphere. The simulation model takes into account the main transitions among the erbium energy levels, the amplified spontaneous emission and the most important secondary transitions pertaining to the ion-ion interactions. The taper angle of the optical fiber and the fiber-microsphere gap have been designed to efficiently inject into the microsphere both the pump and the signal beams and to improve their spatial overlapping with the rare earth doped region. In order to reduce the computational time, a detailed investigation of the amplifier performance has been carried out by changing the number of sectors in which the doped area is partitioned. The simulation results highlight that this scheme could be useful to develop high efficiency and compact mid-infrared amplifiers.

© 2012 Optical Society of America

**OCIS codes:** (230.5750) Optical devices; (140.4480) Lasers and laser optics.

---

## References and links

1. H. C. Ren, F. Vollmer, S. Arnold, and A. Libchaber, "High-Q microsphere biosensor-analysis for adsorption of rodlike bacteria," *Opt. Express* **15**, 17410–17423 (2007).
2. F. Vollmer and A. Stephen, "Whispering-gallery-mode biosensing: label-free detection down to single molecules," *Nat. Methods* **5**, 591–596 (2008).
3. L. Yang and K. J. Vahala, "Gain functionalization of silica microresonators," *Opt. Lett.* **28**, 592–594 (2008).
4. G. S. Murugan, M. N. Zervas, Y. Panitchob, and J. S. Wilkinson, "Integrated Nd-doped borosilicate glass microsphere laser," *Opt. Lett.* **36**, 73–75 (2011).
5. S. Y. Chen, T. Sun, K. T. V. Grattan, K. Annapurna, and R. Sen, "Characteristics of Er and ErYbCr doped phosphate microsphere fibre lasers," *Opt. Commun.* **282**, 3765–3769 (2009).
6. P. Feron, "Whispering Gallery Mode Lasers in Erbium doped fluoride glasses," *Annales de la Fondation Louis de Broglie* **29**, 317–329 (2004).
7. G. Nunzi Conti, A. Chiasera, L. Ghisa, S. Berneschi, M. Brenni, Y. Dumeige, S. Pelli, S. Sebastiani, P. Feron, M. Ferrari, and G. C. Righini, "Spectroscopic and lasing properties of  $\text{Er}^{3+}$  doped glass microspheres," *J. Non-Crystalline Sol.* **352**, 2360–2363 (2006).
8. G. R. Elliot, D. W. Hewak, G. Senthil Murugan, and J. S. Wilkinson, "Chalcogenide glass microspheres; their production, characterization and potential," *Opt. Express* **15**, 17542–17553 (2007).
9. L. Mescia, F. Prudeniano, M. De Sario, T. Palmisano, M. Ferrari, and G. C. Righini, "Design of Rare-Earth-Doped Microspheres," *IEEE Photon. Technol. Lett.* **22**, 422–424 (2010).
10. T. Kouki and T. Makoto, "Optical microsphere amplification system," *Opt. Lett.* **32**, 3197–3199 (2007).
11. Y. G. Boucher and P. Feron, "Generalized transfer function: A simple model applied to active single-mode microring resonators," *Opt. Commun.* **282**, 3940–3947 (2009).

12. F. Prudenzeno, L. Mescia, L. Allegratti, V. Moizan, V. Nazabal, and F. Smektala, "Theoretical study of cascade laser in erbium-doped chalcogenide glass fibers," *Opt. Mat.* **33**, 241–245 (2010).
13. B. E. Little, J. P. Laine, and H. A. Haus, "Analytic Theory of Coupling from Tapered Fibers and Half-Blocks into Microsphere Resonators," *J. Lightwave Technol.* **17**, 704–715 (1999).
14. M. L. Gorodetsky and V. S. Ilchenko, "Optical microsphere resonators: optimal coupling to high-Q whispering-gallery modes" *J. Opt. Soc. Am. B* **16**, 147–154 (1999).
15. C. L. Zou, Y. Yang, C. H. Dong, Y. F. Xiao, X. W. Wu, Z. F. Han, and G. C. Guo, "Taper-microsphere coupling with numerical calculation of coupled-mode theory," *J. Opt. Soc. Am. B* **25**, 1895–1898 (2008).
16. H. A. Haus, *Waves and Fields in Optoelectronics* (Prentice Hall Inc., 1984).
17. M. J. F. Digonnet, *Rare-Earth-Doped Fiber Lasers and Amplifiers* (Marcel Dekker Inc., 2001).
18. K. Vahala, *Optical Microcavities* (World Scientific Publishing, 2004).
19. A. W. Snyder and J. D. Love, *Optical Waveguide Theory* (Chapman and Hall, 1988).
20. J. S. Sanghera and I. D. Aggarwal, "Active and passive chalcogenide glass optical fibers for IR applications: a review," *J. Non-Crystalline Sol.* **256-257**, 6–16 (1999).

## 1. Introduction

During the last decades, the demand for micro-resonators implementing a great variety of photonic devices is rapidly increased. Dielectric micro- and nano-spheres have attracted the research attention since they can transmit very specific (nearly single frequency) wavelengths and the intensity of light inside them can be orders of magnitude higher than that of the incoming light. These spherical microresonators allow light confinement in circling orbits by means of repeated total internal reflections, near the curvilinear boundary. The corresponding modes, called whispering gallery modes (WGMs), exhibit high quality factor  $Q$  (higher than  $10^9$ ) and small mode volume. These properties make WGMs interesting for many applications including the polarization transmission, coupled-resonator-induced transparency, biosensor analysis [1, 2], nonlinear optics, cavity quantum electrodynamics (QED), quantum information processing [3].

The high  $Q$ -factor of micro- and nano-spheres allows the light trapping and strong enhancement of the light-matter interaction. As a consequence, when doped with rare-earth ions, the microsphere can exhibit a lasing action. Until now, laser oscillation has been observed in a variety of rare-earth doped microspheres based on silica, phosphate, tellurite and ZBLAN glass host materials [3–7]. These lasers were characterized by ultralow lasing threshold and very narrow emission linewidths. However, if compared to other technologies exploiting high index materials, the microspheres made of conventional glasses exhibit modal volume several orders of magnitude higher. On the contrary, chalcogenide microspheres are an attractive alternative since their high refractive index ( $2\div 3$ ) leads to lower modal volume as well as high absorption and emission cross sections [8]. The low phonon energy ( $300\div 400\text{ cm}^{-1}$ ) results in large radiative decay rates, high quantum efficiency and allows some radiative transitions which are quenched by the multiphonon decay in silica glasses. Moreover, the high rare earth solubility in a lot of chalcogenide glasses facilitates the fabrication of efficient lasers and amplifiers. Among the advantages related to the use of  $\text{Er}^{3+}$ -doped chalcogenide microspheres there is the prospective to construct a new generation of coherent sources in mid-infrared wavelength range. These sources could be very interesting for a number of applications in the life sciences, spectroscopy, bio-medicine, biological and environmental sensing.

Many papers have been devoted to experimentally demonstrate the capability of the rare earth doped microspheres for generating and amplifying optical signals [3–7], but only few numerical analysis and/or simulation models have been performed [9–11]. Accurate numerical modeling is needed for device performance prediction, design and refinement as well as to obtain peculiar properties that may be exploited in the fabrication of more complex optical systems. In this paper, an accurate mathematical model is implemented and the obtained results encourage the construction of  $\text{Er}^{3+}$ -doped chalcogenide microspheres. The design is

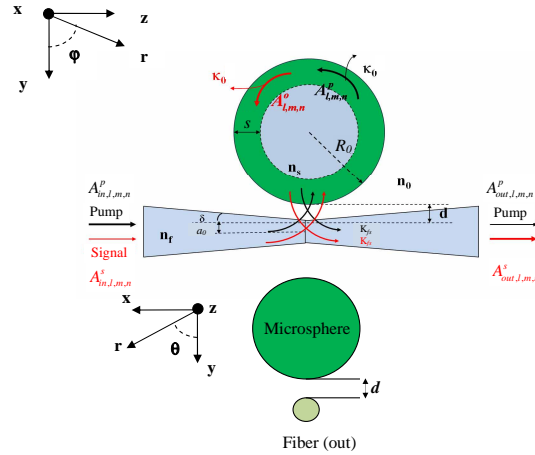


Fig. 1. Layout scheme of the fiber taper coupled to the  $\text{Er}^{3+}$ -doped chalcogenide microsphere.

realistically carried out, on the basis of the optical and spectroscopic parameters measured on chalcogenide glass [12] and by considering the coupling of the microsphere with a tapered fiber. A dedicated 3D numerical code based on the coupled mode theory and solving the rate equations has been developed. In particular, the model includes the modal distribution of the optical waves in both tapered fiber and microsphere, and takes into account the most relevant active phenomena in  $\text{Er}^{3+}$ -doped chalcogenide glasses such as the radiative and nonradiative transition rates, at both pump and signal wavelengths, the stimulated emission of the signal, the amplified spontaneous emission noise (ASE), the lifetime and branching ratios of the considered energy levels, the ion-ion energy transfers and the excited state absorption (ESA). For the first time, WGM amplification in microspherical resonator at  $2.7 \mu\text{m}$  wavelength is accurately modeled by considering important design parameters such as the Q-factor, the spectral range, the loss effects, the mode volume, the coupling characteristics, the buildup factor and the spectroscopic properties of the  $\text{Er}^{3+}$  ions. In particular, a number of simulations has been performed with the aim to identify the optimal geometric parameters leading to the best device performance. The paper is organized as follows: Section 2 gives the theoretical recalls of: i) WGMs propagation, ii) erbium-doped microspheres, iii) coupled mode theory describing the tapered fiber-microsphere system. The results and discussion are provided in Section 3 while conclusions are given in Section 4.

## 2. Theory

Figure 1 shows the layout scheme of the designed resonator. It consists of a tapered optical fiber placed close to the equator of an  $\text{Er}^{3+}$ -doped chalcogenide microsphere. The evanescent field of the optical fiber tunnels in the microsphere and the excitation of WGMs is achieved. Since the fundamental WGMs are localized near the microsphere surface, this coupling technique enables a very efficient excitation without affecting the high Q-factor characteristics. It allows the extraction of the cavity power through the same fiber and the control of the coupling characteristics. Moreover, the tapered fiber allows the focusing and the alignment of the input beam and it efficiently filters the high-order fiber modes. The design of this device requires the use of the electromagnetic mode analysis of both the fiber and the microsphere, the coupled mode theory and the rate equations formalism. In fact, the accurate calculation of the modal electromagnetic field distribution and of the propagation constants of the guided propagation

modes in both the fiber and the microsphere is essential to evaluate the coupling coefficients, the quality factor, the mode volume, the transition rates for modeling the active behavior [13].

The electromagnetic analysis of the microsphere is performed by finding the solution of the scalar Helmholtz equation in spherical coordinates:

$$\frac{1}{r^2 \sin \theta} \left[ \sin \theta \frac{\partial}{\partial r} \left( r^2 \frac{\partial \psi}{\partial r} \right) + \frac{\partial}{\partial \theta} \left( \sin \theta \frac{\partial \psi}{\partial \theta} \right) + \frac{1}{\sin \theta} \frac{\partial^2 \psi}{\partial \varphi^2} \right] + k^2 n_s^2 \psi = 0 \quad (1)$$

where  $k = 2\pi/\lambda$  is the wave vector in vacuum,  $\lambda$  is the wavelength in vacuum and  $n_s$  is the refractive index of the microsphere. In particular, the polarization direction of the electromagnetic field is considered constant along a fixed spherical coordinate. The solution of Eq. (1) is separable, i.e.  $\psi_{l,m,n}(r, \theta, \varphi) = N_s R(r) \Theta(\theta) \Phi(\varphi)$ ; being  $\psi_{l,m,n} = E_\theta$  for the transverse electric (TE) modes, and  $\psi_{l,m,n} = H_\theta$  for the transverse magnetic (TM) modes.  $N_s$  is the normalization constant calculated so that the volume integral of  $\psi_{l,m,n}^2$  over all space, divided by the microsphere circumference is equal to unit [13]. As a consequence, each WGM can be identified by three integers  $l, m, n$  where  $l - m + 1$  is the number of field maxima in the polar,  $\hat{\theta}$ , direction and  $n$  is the number of field maxima along the radial direction.

The azimuthal dependence  $\Phi(\varphi)$  can be expressed in terms of complex exponential functions depending on the mode number  $m \leq l$ . If the sphere radius is larger than the effective wavelength, the WGMs are characterized by large values of  $m$  and  $l$ . Moreover, the approximation  $\theta \ll 1$  for the polar angle has been considered because the corresponding modes are the most strongly coupled with the tapered fiber. In this case, the polar dependence  $\Theta(\theta)$  can be represented by the Hermite polynomials of order  $N = l - m$ . Therefore, the radial solution  $R(r)$  can be expressed in terms of spherical Bessel functions depending on the mode orders  $l$  and  $n$  [13].

By matching the tangential components of electric and magnetic fields at the sphere boundary, the following characteristic equation is obtained [13]:

$$\left( \eta_s \alpha_s + \frac{l}{R_0} \right) j_l(kn_s R_0) = kn_s j_{l+1}(kn_s R_0) \quad (2)$$

where

$$\eta_s = \begin{cases} 1 & \text{TE mode} \\ \frac{n_s^2}{n_0^2} & \text{TM mode} \end{cases} \quad (3)$$

$$\alpha_s = \sqrt{\beta_l^2 - k^2 n_0^2}$$

$$\beta_l = \frac{\sqrt{l(l+1)}}{R_0}$$

$R_0$  is the sphere radius,  $\beta_l$  is the propagation constant parallel to the surface of the microsphere,  $\alpha_s$  is the constant describing the evanescent field decay from the microsphere along the radial direction,  $n_0$  is the background refractive index,  $j_l$  is the spherical Bessel function of the  $l$ -th order. Equation (2) enables the calculation of the resonance wavelengths and their corresponding modal field distributions.

The coupling of the optical power between the tapered fiber and the undoped microsphere is modeled by using the coupled mode theory [14, 15]. In particular, the following hypothesis are used: i) weak coupling, ii) small internal resonator losses, iii) small perturbation of optical fiber and resonator modes, iv) slowly varying amplitude approximation, v) single mode fiber coupled to a WGM of the cavity, vi) adiabatic tapered fiber, vii) coupling zone much smaller

than the microsphere diameter. Owing to these conditions, the time evolution of the amplitude  $A_{l,m,n}$  of the internal cavity electromagnetic field can be obtained by solving the differential equation [14–16]:

$$\frac{dA_{l,m,n}}{dt} = -\frac{1}{2} \left( \frac{1}{\tau_{ext}} + \frac{1}{\tau_0} - 2i\Delta\omega \right) A_{l,m,n} + i\sqrt{\frac{1}{\tau_{ext}\tau}} A_{in} \quad (4)$$

Here,  $A_{in}$  is the amplitude of the input electric field into the coupling region,  $\tau = 2\pi R_0 n_{eff}/c$  is the circulation time inside the microsphere (round trip time),  $n_{eff}$  is the WGM effective refractive index and  $c$  the speed of light in vacuum,  $\Delta\omega = \omega_{in} - \omega_{WGM}$  is the frequency detuning of the fiber input signal from the WGM frequency. The intrinsic lifetime  $\tau_0 = 1/\kappa_0^2 = Q_0/\omega_{WGM}$ , where  $Q_0$  is the intrinsic quality factor and  $\kappa_0$  is the intrinsic cavity decay rate which depends on the total losses due to the material absorption, surface scattering losses, radiative losses and whispering gallery losses [13]. In microspheres having a diameter around a few tens of micron and a perfect surface, both the radiative and surface scattering losses can be neglected.

The coupling lifetime  $\tau_{ext} = 1/\kappa^2 = m\pi/(\omega\kappa_{fs}^2)$ , where  $\kappa$  is the cavity decay rate, denotes the coupling phenomenon between microsphere and optical fiber. In particular, the coupling coefficient  $\kappa_{fs}$  was calculated according to the overlap integral [13]

$$\kappa_{fs} = \int_V \frac{k^2 (n_s^2 - n_0^2)}{2\beta_f} \mathbf{E}_f \cdot \mathbf{E}_s^* dV \quad (5)$$

where  $\mathbf{E}_f$  is the field of the fundamental mode of the optical fiber and  $\mathbf{E}_s$  is the WGM field of the microsphere. Both the electromagnetic fields are calculated by using the Eqs. (1)-(3) and normalizing on the  $\hat{r} \cdot \hat{\theta}$  plane such that

$$\int_0^\pi \int_0^{+\infty} |E_f|^2 r dr d\theta = 1 \quad (6)$$

$$\int_0^\pi \int_0^{+\infty} |E_s|^2 r dr d\theta = 1 \quad (7)$$

In particular, for an adiabatic taper, the fiber radius,  $a$ , can be approximated as

$$a(z) = a_0 + |z| \delta \quad (8)$$

where  $\delta$  is the tapered angle and  $a_0$  is the fiber radius at the waist of the tapered fiber, as shown in Fig. 1. As result, the  $z$ -depending propagation constant,  $\beta_f$ , of the optical fiber mode can be calculated by solving the characteristic equation [13]

$$k_f \frac{J_1[a(z)k_f]}{J_0[a(z)k_f]} = \alpha_f \frac{K_1[a(z)\alpha_f]}{K_0[a(z)\alpha_f]} \quad (9)$$

where

$$k_f = \sqrt{k^2 n_f^2 - \beta_f^2} \quad (10)$$

$$\alpha_f = \sqrt{\beta_f^2 - k^2 n_0^2} \quad (11)$$

$J_v$  and  $K_v$ ,  $v = 0, 1$ , are the Bessel functions of the first kind and the modified Bessel functions of the second kind, respectively.

The interaction of the WGMs with the rare earth doped microsphere has been investigated by using the rate equation model. Figure 2 shows the schematic of six energy manifolds

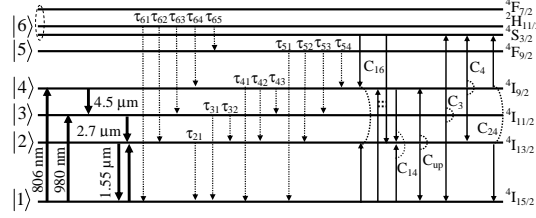


Fig. 2. Energy level diagram of the  $\text{Er}^{3+}$  ions considered in our simulations.

(numbered with  $|i\rangle$   $i = 1, 2, \dots, 6$ ), the electronic transitions and the energy transfers of the trivalent erbium ions in the chalcogenide glass. The state  $|6\rangle$  is constituted by the  ${}^4F_{7/2}$ ,  ${}^2H_{11/2}$ ,  ${}^4F_{9/2}$  manifolds because the nonradiative transition  ${}^4F_{7/2} \rightarrow {}^2H_{11/2}$  is very fast, and the  ${}^4S_{3/2}$  and  ${}^2H_{11/2}$  are thermally distributed. However, the complex  $\text{Er}^{3+}$ -ions system was justified by the fact that in the considered chalcogenide glass the lifetime of the  ${}^4I_{13/2}$ ,  ${}^4I_{11/2}$ ,  ${}^4I_{9/2}$  energy manifolds are comparable and the lifetime of the  ${}^4F_{9/2}$  energy manifolds is small but not negligible. In particular, the important energy exchange processes considered in the model are: 1) both 806 nm ( ${}^4I_{15/2} \rightarrow {}^4I_{9/2}$ ) and 980 nm ( ${}^4I_{15/2} \rightarrow {}^4I_{11/2}$ ) pump transitions, 2) 4.5  $\mu\text{m}$  ( ${}^4I_{9/2} \rightarrow {}^4I_{11/2}$ ), 2.7  $\mu\text{m}$  ( ${}^4I_{11/2} \rightarrow {}^4I_{13/2}$ ) and 1.55  $\mu\text{m}$  ( ${}^4I_{13/2} \rightarrow {}^4I_{15/2}$ ) stimulated emission transitions, 3) different spontaneous decays (point arrows), 4) various types of energy transfer mechanisms occurring in a pair of  $\text{Er}^{3+}$  ions: ( ${}^4I_{13/2}, {}^4I_{13/2} \rightarrow {}^4I_{15/2}, {}^4I_{9/2}$ ), ( ${}^4I_{11/2}, {}^4I_{11/2} \rightarrow {}^4I_{15/2}, {}^4S_{3/2}$ ), ( ${}^4I_{9/2}, {}^4I_{9/2} \rightarrow {}^4S_{3/2}, {}^4I_{13/2}$ ), ( ${}^4I_{15/2}, {}^4I_{9/2} \rightarrow {}^4I_{13/2}$ ), ( ${}^4I_{15/2}, {}^4S_{3/2} \rightarrow {}^4I_{13/2}, {}^4I_{9/2}$ ), ( ${}^4I_{13/2}, {}^4I_{9/2} \rightarrow {}^4I_{15/2}, {}^4S_{3/2}$ ).

The doped area, in the plane  $\hat{r} \cdot \hat{\theta}$  is divided in  $q$  sector, as showed in Fig. 3. In particular,  $\Delta r$  and  $\Delta\theta$  are the radial and polar dimension of each sector,  $S_q$  is the area of the  $q$ -th sector,  $\theta_{\max}$  is the maximum polar angle defining the doped area considered in the simulations.

The rate equations describing the population dynamic of the  $|1\rangle$ – $|6\rangle$  energy manifolds can be written as:

$$\begin{aligned} \frac{dN_1^q}{dt} &= (W_{21}^q + C_{up}N_2^q + C_{24}N_4^q + A_{21})N_2^q + (C_3N_3^q + A_{31})N_3^q + A_{41}N_4^q + A_{51}N_5^q + A_{61}N_6^q + \\ &\quad - (R_{13}^q + R_{14}^q + W_{12}^q + 2C_{16}N_6^q + C_{14}N_4^q)N_1^q \\ \frac{dN_2^q}{dt} &= (W_{12}^q + 2C_{16}N_6^q + C_{14}N_4^q)N_1^q + (W_{32}^q + A_{32})N_3^q + (C_{14}N_1^q + C_4N_4^q + A_{42})N_4^q + A_{52}N_5^q + \\ &\quad + A_{62}N_6^q - (W_{21}^q + C_{24}N_4^q + 2C_{up}N_2^q + A_{21})N_2^q \\ \frac{dN_3^q}{dt} &= R_{13}^qN_1^q + A_{43}N_4^q + A_{53}N_5^q + A_{63}N_6^q - (W_{32}^q + 2C_3N_3^q + A_{31} + A_{32})N_3^q \\ \frac{dN_4^q}{dt} &= 2C_{16}N_1^qN_6^q + C_{up}(N_2^q)^2 - (A_{41} + A_{42} + A_{43} + C_{14}N_1^q + 2C_4N_4^q + C_{24}N_2^q)N_4^q + \\ &\quad + A_{54}N_5^q + A_{64}N_6^q + R_{14}^qN_1 \\ \frac{dN_5^q}{dt} &= A_{65}N_6^q - (A_{51} + A_{52} + A_{53} + A_{54})N_5^q \\ \frac{dN_6^q}{dt} &= C_3(N_3^q)^2 + C_4(N_4^q)^2 + C_{24}N_2^qN_4^q - (A_{61} + A_{62} + A_{63} + A_{64} + A_{65} + 2C_{16}N_1^q)N_6^q \end{aligned}$$

where  $N_i^q$   $i = 1, 2, \dots, 6$  is the concentration of  $i$ -th energy manifold in the  $q$ -th sector,  $R_{ij}^q$  is the pump transition rate and  $W_{ij}^q$  is the signal transition rate in the  $q$ -th sector defined as:

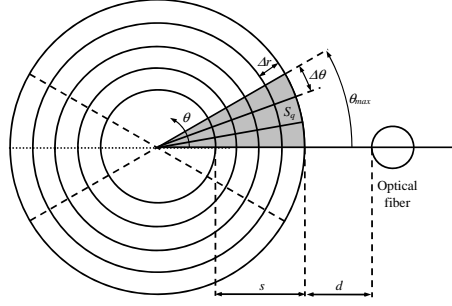


Fig. 3. Discretization of the doped area in the plane  $\hat{r} \cdot \hat{\theta}$ .

$$R_{ij}^q = \sum_{l,m,n} R_{ij}^{q,l,m,n}$$

$$W_{ij}^q = \sum_{l,m,n} W_{ij}^{q,l,m,n}$$

$R_{ij}^{q,l,m,n}$  and  $W_{ij}^{q,l,m,n}$  are the contribution to the pump and signal rate of each WGM propagating into the microsphere and they can be calculated as

$$R_{ij}^{q,l,m,n} = \frac{\sigma_{ij}(\tilde{\nu})}{h\tilde{\nu}S_q} \int \int_{S_q} I_{l,m,n}^p(r, \theta, \varphi = 0, t) r dr d\theta \quad (12)$$

$$W_{ij}^{q,l,m,n} = \frac{\sigma_{ij}(\tilde{\nu})}{h\tilde{\nu}S_q} \int \int_{S_q} I_{l,m,n}^s(r, \theta, \varphi = 0, t) r dr d\theta \quad (13)$$

where  $\tilde{\nu} = \nu_{l,m,n}$  is the WGM resonant frequency,  $\sigma_{i,j}(\tilde{\nu})$  is the emission cross section at the frequency  $\tilde{\nu}$ , when  $i > j$ , and the absorption cross section at the frequency  $\tilde{\nu}$  when  $i < j$ , and  $(1/S_q) \int \int_{S_q} I_{l,m,n}^{s,p} r dr d\theta$  is the average value, over the doped area  $S_q$ , of the intensity profile. In particular, the intensity profile at pump,  $I_{l,m,n}^p$ , and signal,  $I_{l,m,n}^s$ , frequency can be formulated in terms of electric field by [15]:

$$I_{l,m,n}^a(r, \theta, \varphi, t) = \frac{1}{2} \epsilon_0 c n_{eff}(\tilde{\nu}) |A_{l,m,n}^a(\varphi, t)|^2 |E_{l,m,n}^a(r, \theta)|^2 \quad \text{with } a = p, s \quad (14)$$

$A_{l,m,n}^a(\varphi, t)$  is the slowly varying amplitude and  $E_{l,m,n}^a(r, \theta)$  is the normalized electric field on the plane  $\hat{r} \cdot \hat{\theta}$ . Thus, the Eqs. (12)-(13) can be written as

$$R_{ij}^{q,l,m,n} = \frac{\sigma_{ij}(\tilde{\nu})}{2\tilde{\nu}hS_q} \epsilon_0 c n_{eff}(\tilde{\nu}) |A_{l,m,n}^p(\varphi = 0, t)|^2 \Gamma_{l,m,n}^{q,p} \quad (15)$$

$$W_{ij}^{q,l,m,n} = \frac{\sigma_{ij}(\tilde{\nu})}{2\tilde{\nu}hS_q} \epsilon_0 c n_{eff}(\tilde{\nu}) |A_{l,m,n}^s(\varphi = 0, t)|^2 \Gamma_{l,m,n}^{q,s} \quad (16)$$

where

$$\Gamma_{l,m,n}^{q,a} = \int \int_{S_q} |E_{l,m,n}^a(r, \theta)|^2 r dr d\theta \quad \text{with } a = p, s \quad (17)$$

is the overlap factor of each WGM with the rare-earth profile in the  $q$ -th sector. The condition  $\varphi = 0$  in Eqs. (15)-(16) is used by considering that the azimuthal dependence of the electromagnetic field takes the form  $\exp(-jm\varphi)$ .



By describing the amplified spontaneous emission (ASE) via the theory reported in [17], and by taking into account the Eqs. (13) and (17) and the variable change  $d\phi = (c/n_{eff}) dt$  the differential equation governing the evolution of the amplitude of both the pump and the ASE within the doped microsphere can be expressed as:

$$\begin{aligned}\frac{dA_{l,m,n}^p}{dt} &= \frac{c}{2n_{eff}} \left[ \sum_q N_j^q \sigma_{ji}(\tilde{\nu}) \Gamma_{l,m,n}^{q,p} - \sum_q N_i^q \sigma_{ij}(\tilde{\nu}) \Gamma_{l,m,n}^{q,p} \right] A_{l,m,n}^p \quad \text{with } i < j \\ \frac{dA_{l,m,n}^s}{dt} &= \frac{c}{2n_{eff}} \left\{ \sum_q N_j^q \sigma_{ji}(\tilde{\nu}) \Gamma_{l,m,n}^{q,s} [A_{l,m,n}^s + A_0] - \sum_q N_i^q \sigma_{ij}(\tilde{\nu}) \Gamma_{l,m,n}^{q,s} A_{l,m,n}^s \right\} \quad \text{with } i < j\end{aligned}\quad (18)$$

$A_0 = (2h\tilde{\nu}\Delta\nu)/(A_{l,m,n}^s c n_{eff} \epsilon_0)$  being the equivalent input noise corresponding to one photon per whispering gallery mode in the bandwidth  $\Delta\nu$  [17].

Since the obtained differential Eqs. (18) are of the same kind of the equation (4), a term concerning the light-matter interaction can be added to obtain:

$$\begin{aligned}\frac{dA_{l,m,n}^p}{dt} &= -\frac{1}{2} \left( \frac{1}{\tau_{ext}} + \frac{1}{\tau_0} - g_{l,m,n}^p - 2i\Delta\omega \right) A_{l,m,n}^p + i\sqrt{\frac{1}{\tau_{ext}\tau}} A_{in,l,m,n}^p \\ \frac{dA_{l,m,n}^s}{dt} &= -\frac{1}{2} \left( \frac{1}{\tau_{ext}} + \frac{1}{\tau_0} - g_{l,m,n}^s - 2i\Delta\omega \right) A_{l,m,n}^s + \frac{c}{2n_{eff}} \sum_q N_j^q \sigma_{ji}(\tilde{\nu}) \Gamma_{l,m,n}^{q,s} A_0 + \\ &\quad + i\sqrt{\frac{1}{\tau_{ext}\tau}} A_{in,l,m,n}^s\end{aligned}\quad (19)$$

where the term

$$g_{l,m,n}^a = \frac{c}{n_{eff}} \left( \sum_q N_j^q \sigma_{ji}(\tilde{\nu}) \Gamma_{l,m,n}^{q,a} - \sum_q N_i^q \sigma_{ij}(\tilde{\nu}) \Gamma_{l,m,n}^{q,a} \right) \quad \text{with } a = p, s \quad (20)$$

arises from the interaction of both the optical pump and the signal to be amplified with  $\text{Er}^{3+}$  ions. In particular, if the laser action occurs  $g_{l,m,n}^p < 0$  describes the decay of the pump energy and  $g_{l,m,n}^s > 0$  quantifies the energy improvement of the WGM. Finally, the overall transmittance can be expressed by the equation [18]

$$T = \left| \frac{A_{out,l,m,n}^a}{A_{in,l,m,n}^a} \right|^2 = \left| \sqrt{1 - \frac{\tau}{\tau_{ext}}} + i\sqrt{\frac{\tau}{\tau_{ext}}} \frac{A_{l,m,n}^a}{A_{in,l,m,n}^a} \right|^2 \quad \text{with } a = p, s \quad (21)$$

where the resonance character of the transmittance becomes apparent when the dependence of  $\tau$ ,  $\tau_{ext}$ ,  $A_{l,m,n}^a$  and  $A_{in,l,m,n}^a$  on the WGM resonance frequency  $\tilde{\nu}$  is considered.

### 3. Numerical results

The numerical investigation is aimed to the evaluation of  $\text{Ga}_5\text{Ge}_{20}\text{Sb}_{10}\text{S}_{65}$  chalcogenide glass feasibility for the construction of microsphere amplifiers operating in the mid-infrared wavelength range. In order to carry out a realistic design, the simulations have been performed by taking into account the refractive index wavelength dispersion [12] and the spectroscopic parameter summarized in Table 1. Moreover, a very short lifetime ( $10^{-6}$  s) of the state  $|6\rangle$  and transition rates  $A_{61} = A_{62} = A_{63} = A_{64} = 0$  have been considered in the calculations.

In order to overcome the limitations due to the dense optical spectrum of WGMs, a quite small microsphere has been considered. Figure 4 shows the transmission characteristic around



Table 1. Spectroscopic parameters of the  $\text{Er}^{3+}$ -doped chalcogenide microsphere.

Transitions	Wavelength $\lambda$ (nm)	Transition Probability (%)	Ion Lifetime (ms)	Emission cross section ( $\text{m}^2$ )	Absorption cross section ( $\text{m}^2$ )
$^4I_{13/2} \rightarrow ^4I_{15/2}$	1531.7	$\beta_{21} = 100$	$\tau_{21} = 1.83$	-	-
$^4I_{11/2} \rightarrow ^4I_{15/2}$	986.4	$\beta_{31} = 86.28$	$\tau_{31} = 1.37$	0	$1.32 \times 10^{-24}$
$^4I_{11/2} \rightarrow ^4I_{13/2}$	2770.7	$\beta_{32} = 13.72$	$\tau_{32} = 1.37$	$1.4 \times 10^{-24}$	0
$^4I_{9/2} \rightarrow ^4I_{15/2}$	810.0	$\beta_{41} = 80.38$	$\tau_{41} = 1.08$	-	-
$^4I_{9/2} \rightarrow ^4I_{13/2}$	1719.1	$\beta_{42} = 18.82$	$\tau_{42} = 1.08$	-	-
$^4I_{9/2} \rightarrow ^4I_{11/2}$	4529.4	$\beta_{43} = 0.80$	$\tau_{43} = 1.08$	-	-
$^4F_{9/2} \rightarrow ^4I_{15/2}$	662.7	$\beta_{51} = 91.99$	$\tau_{51} = 0.13$	-	-
$^4F_{9/2} \rightarrow ^4I_{13/2}$	1168.1	$\beta_{52} = 4.32$	$\tau_{52} = 0.13$	-	-
$^4F_{9/2} \rightarrow ^4I_{11/2}$	2019.4	$\beta_{53} = 3.34$	$\tau_{53} = 0.13$	-	-
$^4F_{9/2} \rightarrow ^4I_{9/2}$	3623.1	$\beta_{54} = 0.35$	$\tau_{54} = 0.13$	-	-

(a) pump wavelength  $\lambda_p = 0.98 \mu\text{m}$  and (b) signal wavelength  $\lambda_s = 2.76 \mu\text{m}$ , of the undoped microsphere coupled with the tapered fiber by considering sphere radius  $R_0 = 25 \mu\text{m}$  and taper-microsphere gap  $d = 460 \text{ nm}$ , at the pump wavelength, and  $d = 1.8 \mu\text{m}$ , at the signal wavelength. The different values of  $d$  have been chosen to obtain the critical coupling condition at both wavelengths. The size of the fiber taper has been designed to ensure the fundamental mode propagation along the waveguide formed by the fiber waist surrounded by air, and to have a significant evanescent field into the space surrounding the taper. In particular, the considered waist radius and taper angle numerical values are  $a_0 = 700 \text{ nm}$  and  $\delta = 0.03 \text{ rad}$ , respectively.

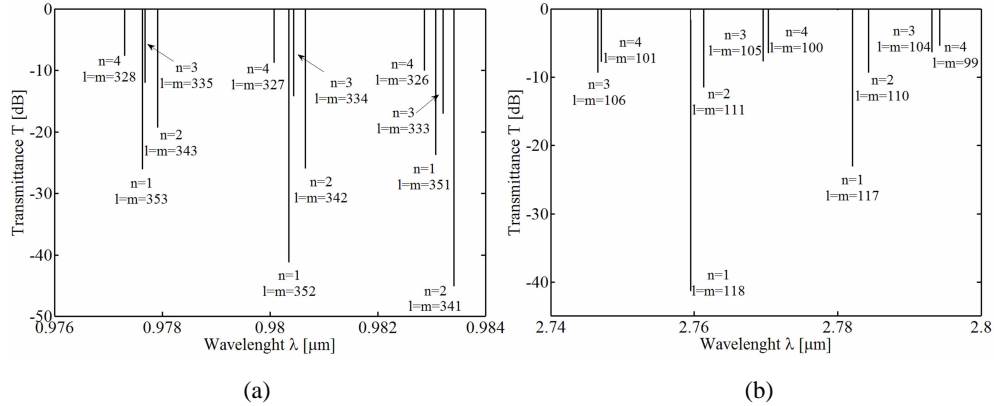


Fig. 4. Transmission spectrum of the undoped microsphere, having radius  $R_0 = 25 \mu\text{m}$ , around (a) pump wavelength  $\lambda_p = 0.98 \mu\text{m}$  and (b) signal wavelength  $\lambda_s = 2.76 \mu\text{m}$ .

The WGM resonances and the coupling coefficients have been determined by numerically solving Eq. (2) and Eq. (5), respectively. In particular, the overlap integral is evaluated by integrating over the transverse plane and along the  $z$  direction so that the volume  $V$  includes only the sphere. In the calculation, the WGM electromagnetic field has been evaluated by solving Eq. (1) and considering the equations of radial, polar and azimuthal dependence reported in [13]. The electromagnetic field and the  $z$ -depending propagation constant of the tapered fiber have been calculated by using the local modal theory [19] and solving Eqs. (9)-(11). Figure 4(a) and Fig. 4(b) show that a lot of modes can be coupled into the microsphere within the pump and signal spectral range. In particular, we have considered a pump wavelength  $\lambda_p = 0.98 \mu\text{m}$  and

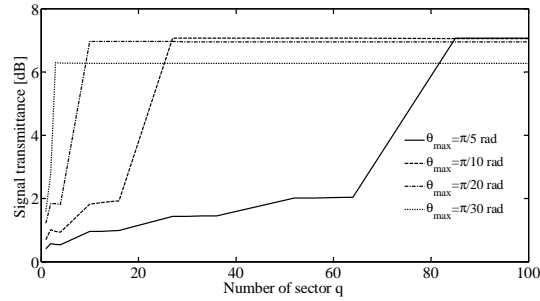


Fig. 5. Signal transmittance versus the number of the sector  $q$  for different maximum polar angles:  $\theta_{max} = \pi/5$  rad (full curve),  $\theta_{max} = \pi/10$  rad (dash curve),  $\theta_{max} = \pi/20$  rad (dash-dot curve) and  $\theta_{max} = \pi/30$  rad (dot curve).

signal wavelength  $\lambda_s = 2.76 \mu\text{m}$  exciting the fundamental WGMs mode  $n = 1$ ,  $m = l = 352$  and  $n = 1$ ,  $m = l = 118$ , respectively.

The main aspect of the numerical simulation pertains to the suitable choice of the sector number  $q$  ensuring a good compromise between the result accuracy and the computational time. Figure 5 summarizes the obtained results regarding the variation of the signal transmittance versus the sector number for different maximum polar angles,  $\theta_{max}$ . In the simulations, the thickness of the erbium-doped region and erbium concentration are  $s = 3 \mu\text{m}$  and  $N_{Er} = 0.5$  w%, respectively. Other parameters are: input pump power  $P_p = 100$  mW, input signal power  $P_s = -50$  dBm, taper angle  $\delta = 0.03$  rad, taper-microsphere gap  $d = 560$  nm, waist radius  $a_0 = 700$  nm. It can be observed that for sectors number higher than 80, the transmittance is almost constant even by increasing  $\theta_{max}$ . This occurrence can be explained by considering that, for small  $\theta_{max}$ , only a part of the power distribution is taken into account in the calculation of the gain. By increasing  $\theta_{max}$ , the tails of the electromagnetic field along the polar direction are also considered for the signal amplification. For  $\theta_{max} > \pi/10$  and  $q > 80$ , the transmittance slightly changes because the electromagnetic field distribution of the fundamental WGM on the  $\hat{r} \cdot \hat{\theta}$  plane is almost completely considered in the calculations. Significant transmittance variation can be observed for  $\theta_{max} > \pi/5$  and  $q < 80$  because a poor sampling of the electromagnetic field occurs. However, we have selected  $\theta_{max} = \pi/10$  and  $q = 30$  since the obtained signal transmittance is practically equal to that calculated for  $\theta_{max} = \pi/5$  and  $q > 80$ .

The variation of the amplifier characteristics due to the changes of the erbium-doped region thickness has been investigated, too. Figure 6 shows the dependence of the signal transmittance as a function of doped region thickness for different maximum polar angles. Other parameters used in the computation are: input pump power  $P_p = 100$  mW, input signal power  $P_s = -50$  dBm, taper angle  $\delta = 0.03$  rad, taper-microsphere gap  $d = 560$  nm, erbium concentration  $N_{Er} = 0.5$  w%, waist radius  $a_0 = 700$  nm. In all the investigated cases, the transmittance increases by increasing the thickness  $s$  of the doped region because a better overlap between WGM electromagnetic field profile and the region containing the erbium ions occurs. For thicknesses of the doped region higher than  $2 \mu\text{m}$  the transmittance is quite constant because the WGM field intensity at both pump and signal wavelengths are bounded in a spatial region enclosed in  $s < 2 \mu\text{m}$ . Nevertheless, the transmittance increases by increasing the maximum polar angles  $\theta_{max}$  till  $\theta_{max} > \pi/10$ . The curves  $\theta_{max} = \pi/5$  and  $\theta_{max} = \pi/10$  are practically unnoticeable.

Figure 7 depicts the transmittance as a function of maximum polar angle  $\theta_{max}$  for three different doped region thicknesses,  $s=1,2,3 \mu\text{m}$ . As expected, for  $\theta_{max} > 0.2$  rad the signal transmittance slightly changes by changing the thickness of the doped region. Thus, according with the aforesaid remarks, the sector number  $q = 30$ , maximum polar angle  $\theta_{max} = \pi/10$  rad,

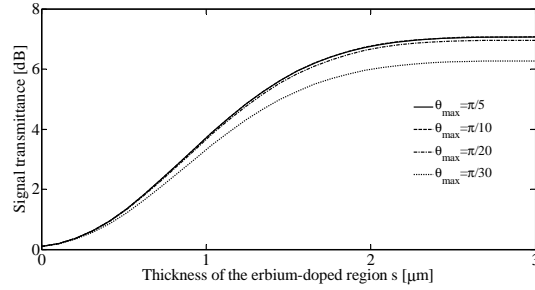


Fig. 6. Signal transmittance versus the thickness of the doped region  $s$  for different maximum polar angles:  $\theta_{max} = \pi/5$  rad (full curve),  $\theta_{max} = \pi/10$  rad (dash curve),  $\theta_{max} = \pi/20$  rad (dash-dot curve) and  $\theta_{max} = \pi/30$  rad (dot curve).

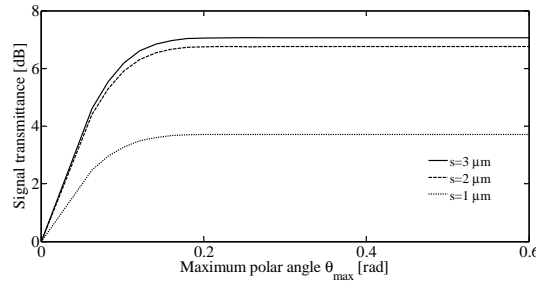


Fig. 7. Signal transmittance versus the maximum polar angle for different thicknesses of the doped region:  $s=3 \mu\text{m}$  (full curve),  $s=2 \mu\text{m}$  (dash curve), and  $s=1 \mu\text{m}$  (dot curve).

thickness of the doped region  $s=3 \mu\text{m}$ , sphere radius  $R_0 = 25 \mu\text{m}$  are fixed in the following simulations, allowing to obtain a good result precision without too much computational time consumption.

The performance of the gain-functionalized microsphere depends on the coupling strength between fiber modes and WGMs and it exhibits different behavior for the under-coupling, over-coupling and critical coupling conditions. In particular, an efficient coupling can be obtained if significant overlap and phase-matching (phase synchronism) between the propagation constant of WGM and the propagation constant of the fundamental taper mode is fulfilled, as well as the frequency of the excitation is resonant with the WGM frequency. To this aim, the taper angle, the fiber radius and the fiber-microsphere gap have been tailored in order to efficiently couple the pump beam into the rare earth-doped microsphere and to enhance the extraction of the amplified signal from the microsphere. Figure 8 shows the transmittance versus the fibre-microsphere gap for different erbium concentration, with taper angle  $\delta = 0.03$  rad and input pump power  $P_p = 100$  mW. The transmittance (marked curves) at both pump and signal wavelengths for the undoped sphere are reported for a comparison. Good signal amplification is obtained for a fibre-microsphere gap close to 500 nm where the condition of critical coupling at the pump wavelength occurs. In fact, in this operational regime the most part of the pump signal is coupled into the microsphere. As result, a strong pump absorption rate occurs, the erbium ions are inverted and the signal stimulated emission rate takes place. It can be also observed that the amplifier performance depends on the erbium concentration. When the fiber is very close to the microsphere ( $d \cong 200$  nm) both the pump and signal to be amplified are in a regime where the coupling is stronger than the loss (over-coupling). In this condition, the energy circulating in the microsphere poorly interacts with the active ions because a large portion of its is

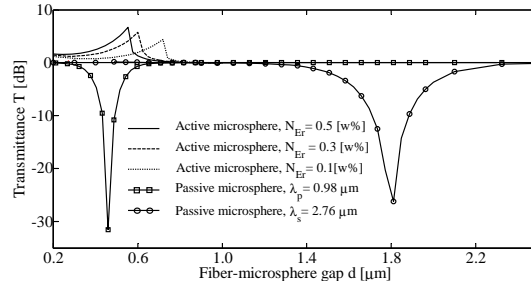


Fig. 8. Transmittance versus the fibre-microsphere gap for different erbium concentrations:  $N_{Er} = 0.5$  w% (full curve),  $N_{Er} = 0.3$  w% (dash curve), and  $N_{Er} = 0.1$  w% (dot curve); transmittance of the undoped microsphere at pump wavelength (square mark) and at signal wavelength (circular mark).

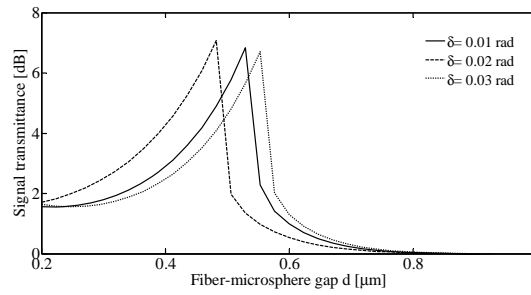


Fig. 9. Signal transmittance versus the fibre-microsphere gap for different taper angles:  $\delta = 0.01$  rad (full curve),  $\delta = 0.02$  rad (dash curve), and  $\delta = 0.03$  rad (dot curve).

coupled out to the fiber. By increasing the gap up to about 550 nm the pump signal circulating in the microsphere is high enough to ensure a strong population inversion whose value mainly depends on erbium concentration. In under-coupling regime ( $d > 550$  nm) only a small part of input pump power is coupled in the microsphere. As result, the reduction of the population inversion due to the ion-ion interaction becomes stronger at higher erbium concentration causing a decreasing of the amplifier performance. Finally, for large gap values the signal amplification cannot be fulfilled because the pump signal in the microsphere is too much low. Figure 9 shows the signal transmittance versus the fibre-microsphere gap for three different taper angles, erbium concentration  $N_{Er} = 0.5$  w%, input pump and signal power  $P_p(0) = 100$  mW and  $P_s(0) = -50$  dBm, respectively. It can be observed that quite similar performance in terms of maximum signal amplification are obtained.

The effect of the pump power on the gain performance is an important issue for the microsphere amplifier. To this aim, Fig. 10 illustrates the transmittance as a function of the input pump power for three different input signal powers. In all the cases, the transmittance linearly increases by increasing the pump power up to a threshold value depending on input signal power:  $\approx 67$  mW for  $P_s = -30$  dBm,  $\approx 78$  mW for  $P_s = -40$  dBm and  $P_s = -50$  dBm. In fact, for input pump power lower than the threshold one the absorption and the stimulated emission rates due to the internal cavity field at the pump and signal wavelength respectively, induce a weak population improvement of the  $^4I_{11/2}$  energy manifold. The different values of the threshold pump power can be explained by taking into account the upconversion phenomena from  $^4I_{13/2}$  and  $^4I_{11/2}$  energy manifolds. In fact, with lower signal power the ion population of the  $^4I_{11/2}$  energy manifold is quite high and the upconversion is more efficient. At the same time,

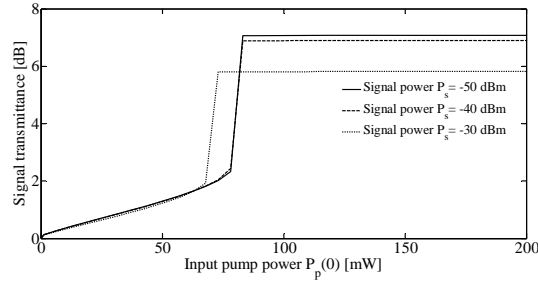


Fig. 10. Signal transmittance versus the pump power for different input signal powers:  $P_s = -50$  dBm (full curve),  $P_s = -40$  dBm (dash curve), and  $P_s = -30$  dBm (dot curve).

the ion population of the  $^4I_{13/2}$  energy manifold is not high enough to compensate the deleterious effect of the upconversion from the  $^4I_{11/2}$  energy manifold. As result, in order to fully invert the active medium higher pump power is required. On the contrary, for input pump powers higher than the threshold one the population of the  $^4I_{11/2}$  energy manifold steeply increases and a strong population inversion occurs. Finally, for input pump power higher than 85 mW the transmittance is, in all the three cases, quite constant because this regime corresponds to a fully inverted medium. Moreover, as expected, the transmittance value decreases by increasing the input signal power, because the gain saturation due to the amplified signal occurs.

Finally, Fig. 11 shows the simulation of the signal transmittance versus the time by considering a constant input signal power,  $P_s = -50$  dBm, and for three different input pump powers. With respect to the steady operation an overshoot is observed which is narrowed by increasing the input pump power. The delay time of the peak corresponding to the lower input pump power is due to a slower dynamic of the absorption pump rate. Moreover, the absence of the spike for  $P_p = 50$  mW can be explained by considering that the pump absorption and stimulated emission rates grow in the same way during the time. The obtained numerical results show that the time constants of the transient gain dynamic depend on the input pump power and, the saturation and recovery times are typically less than few ms.

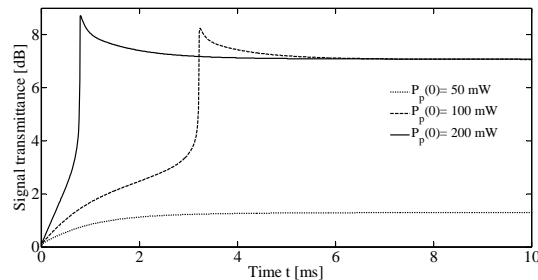


Fig. 11. Signal transmittance versus the time for different input pump powers:  $P_p = 200$  mW (full curve),  $P_p = 100$  mW (dash curve), and  $P_p = 50$  mW (dot curve).

In order to evaluate the effects of the lasing action on the amplifier performance some simulations have been performed by using over 120 WGMs in the wavelength band from 2740 nm to 2780 nm. A laser threshold of about 60 mW and a negligible power of the higher order WGMs have been calculated for input pump power lower than 120 mW. Moreover, higher input pump power can activate the laser action of the high order WGMs in the signal wavelength band without drastically reduce the gain at the signal frequency ( $n=1$ ,  $m=118$ ).

The proposed device is feasible also with reference to the temperature variation, due to the pump power, lower than 50 °C. In fact, by considering typical values of the thermal expansion coefficient ( $\text{CTE}=14.4 \times 10^{-6} \text{ }^{\circ}\text{C}^{-1}$ ) and thermal refraction coefficients ( $\text{dn}_s/\text{dT}=10^{-5} \text{ }^{\circ}\text{C}^{-1}$ ) of chalcogenide glasses [20], a red shift of the pump and signal resonance frequencies of about 0.2 nm and 0.5 nm, respectively, has been calculated for a temperature improvement of 50 °C. These red shifts slowly change the output power at the signal wavelength.

#### 4. Conclusion

In this paper, we have reported an extremely accurate design of  $\text{Er}^{3+}$ -doped chalcogenide microsphere amplifier evanescently coupled with a tapered optical fiber. The device performance has been investigated by changing the fiber-microsphere gap, the thickness of erbium doped region, the fiber taper angle, the erbium concentration and the operative parameters such as pump and signal power. A dedicated 3D model based on coupled mode theory and solving the rate equations has been developed and implemented in a home-made computer code. The electromagnetic analysis of the microsphere has been performed by finding the solution of the scalar Helmholtz equation in spherical coordinates. Moreover, peculiar parameters as quality factor and coupling coefficients have been evaluated by considering the calculated electromagnetic field profile of both microsphere and tapered optical fiber. A detailed analysis pertaining to the simulation accuracy has been performed by changing the amplitude of the computational domain and the number of the discretization points. In particular, sector number  $q=30$  and maximum polar angle  $\theta_{\max} = \pi/10$  rad ensure good result precision and not too much computational time consuming. A significant signal amplification can be obtained for input pump powers higher than 80 mW and, in the small signal operation, maximum optical gain of about 7 dB has been calculated. The performed simulations indicate that the proposed  $\text{Er}^{3+}$ -doped microspheres are good candidates for an efficient frequency-selective amplification, e.g. to restore signal attenuation and to be employed for compact integration of the active optical functionalities.